


Multiscale modeling of gas flow behaviors in nanoporous shale matrix considering multiple transport mechanisms

Wenning Zhou ^{1,2,*} Xu Yang,¹ and Xunliang Liu^{1,2}

¹*School of Energy and Environmental Engineering, University of Science and Technology Beijing, Beijing 100083, China*

²*Beijing Key Laboratory of Energy Conservation and Emission Reduction for Metallurgical Industry, Beijing 100083, China*



(Received 3 January 2022; revised 29 April 2022; accepted 4 May 2022; published 25 May 2022)

This study proposes a multiscale model combining molecular simulation and the lattice Boltzmann method (LBM) to explore gas flow behaviors with multiple transport mechanisms in nanoporous media of shale matrix. The gas adsorption characteristics in shale nanopores are first investigated by molecular simulations, which are then integrated and upscaled into the LBM model through a local adsorption density parameter. In order to adapt to high Knudsen number and nanoporous shale matrix, a multiple-relaxation-time pore-scale LBM model with a regularization procedure is developed. The combination of bounce-back and full diffusive boundary condition is adopted to take account of gas slippage and surface diffusion induced by gas adsorption. Molecular simulation results at the atomic scale show that gas adsorption behaviors are greatly affected by the pressure and pore size of the shale organic nanopore. At the pore scale, the gas transport behaviors with multiple transport mechanisms in nanoporous shale matrix are explored by the developed multiscale model. Simulation results indicate that pressure exhibits more significant influences on the transport behaviors of shale gas than temperature does. Compared with porosity, the average pore size of nanoporous shale matrix plays a more significant role in determining the apparent permeability of gas transport. The roles of the gas adsorption layer and surface diffusion in shale gas transport are discussed. It is observed that under low pressure, the gas adsorption layer has a positive influence on gas transport in shale matrix due to the strong surface diffusion effect. The nanoporous structure with the anisotropy characteristic parallel to the flow direction can enhance gas transport in shale matrix. The obtained results may provide underlying and comprehensive understanding of gas flow behaviors considering multiple transport mechanisms in shale matrix. Also, the proposed multiscale model can be considered as a powerful tool to investigate the multiscale and multiphysical flow behaviors in porous media.

DOI: [10.1103/PhysRevE.105.055308](https://doi.org/10.1103/PhysRevE.105.055308)

I. INTRODUCTION

With the application of horizontal drilling and hydraulic fracturing technology into tight oil and gas reservoirs, the unconventional shale gas resource has been successfully extracted, thereby largely alleviating the energy shortage [1]. Unlike conventional coal and oil resources, the main component of shale gas is methane which belongs to clean fuels and ecofriendly energy. However, the characteristics of unconventional shale gas reservoirs are highly different from traditional gas reservoirs, such as extremely low porosity and permeability, complex and multiscale pore structure network, coexistence of adsorbed gas, dissolved gas as well as free gas, and so forth [2]. Previous studies have shown that the multiscale pores could lead to complicated multiple transport mechanisms of shale gas, including surface diffusion induced by adsorbed gas, Knudsen diffusion, slip flow, and free gas flow [3,4]. For instance, shale gas transport could be affected from two aspects due to the existence of adsorbed gas. On the one hand, the part of the pore volume occupied by the adsorbed gas molecules could reduce the transport space for free gas. On the other hand, the surface diffusion of adsorbed

gas molecules on a solid wall could enhance the transport capacity of shale gas in the micropore [5]. In addition, a shale gas reservoir, composed of inorganic matter (IM), organic matter (OM), and interparticle pores and fractures, is a typical heterogeneous and anisotropic porous structure [6]. Therefore, gas transport in shale reservoirs influenced by these above-mentioned characteristics has been an extremely complicated multiscale and multiphysical field coupling problem.

It is well accepted that the Knudsen number, which is the ratio of mean free path over the characteristic length $Kn = \lambda/h$, is the key parameter for describing flow behaviors. According to the Knudsen number, gas flow is typically classified into four regions, i.e., continuum, slip, transition, and free-molecular flow [7]. Experimental results have shown that the pressure of a shale reservoir is relatively high and the primary pores of the shale OM network are micro- and mesopores with the average pore size less than 50 nm [8]. In this situation, shale gas flow is in slip and early transition flow regimes. Consequently, conventional computational fluid dynamics (CFD) methods based on continuum hypothesis are not applicable. For gas adsorption and transport in the microscale and nanoscale pores, molecular simulation has been an effective method to explore the underlying interactions between gas molecules and solid surfaces [9,10]. In our previous studies, the adsorption behaviors of pure methane and

*wenningzhou@ustb.edu.cn

a gas mixture in organic and inorganic nanopores of shale matrix have been examined by molecular simulations [11–13]. The calculated density distribution profiles indicated that the properties of gas adsorption are greatly affected by the specific composition, temperature, and pressure as well as pore size of shale nanopores. More relative studies regarding gas adsorption and diffusion performance by molecular simulation can be found in the recent review articles [14,15]. However, due to the limitations of computing resources, the scale of molecular simulation is only limited to nanometers and nanoseconds. Thus, numerical models at a larger scale are necessary for the realistic applications of shale gas recovery.

Originating from kinetic theory, the lattice Boltzmann method (LBM) has emerged as a powerful tool for modeling and simulating complex physical problems [16,17]. In recent years, the LBM has been extensively applied for numerical simulation of microscale flow in complex geometry [18–20]. Given the scale of the studied physical problems, the LBM models for porous structure can be divided into two categories, that is, representative elementary volume (REV) scale and pore-scale LBM model [21]. Guo and Zhao [22] developed a REV-scale LBM model for isothermal incompressible flow in porous structures, which incorporated the porosity and drag effects of a porous medium into the model. Their results showed the nonlinear drag force has significant influences for high-speed flows. Based on this model, Chen and co-workers [23] further proposed a REV-scale LB model coupled with gas slippage effect, i.e., Klinkenberg's effect, in which the permeability in the force term was replaced by the apparent permeability modified by Beskok and Karniadakis-Civan's correlation [24,25]. They claimed that gas slippage is a crucial transport mode at large Knudsen number in porous media. However, the models at REV scale do not consider the detailed structure but only focus on the macroscopic parameters of volume average such as porosity [26]. The scale of shale organic matter is relatively small, and gas adsorption and diffusion effects in shale nanopores cannot be ignored. Thus, the pore-scale LB model has advantages in exploring the detailed flow information of pores and in-depth analysis of shale gas flow behaviors.

Over the past decade, researchers have made great efforts in modeling multiphysical phenomena in porous media by developing pore-scale LBM models. Ning *et al.* [27] proposed a multiple-relaxation-time (MRT) LBM model taking account of slippage and adsorption effects and calculated the apparent permeability in shale porous structures with different porosities. They argued that the increasing adsorption strength could reduce the apparent permeability of shale gas. Ren *et al.* [28] subsequently developed a diffuse-bounce-back boundary condition to incorporate the influence of surface diffusion, where the surface diffusion of adsorbed gas molecules was regarded as a moving solid wall. Taking into consideration slippage effect and local characteristic length, Wang *et al.* [26] focused on the influences of porosity and specific surface area on apparent permeability under different pressures. Their results demonstrated the importance of the structural information of porous media on flow behaviors. Zhang and Sun [29] formulated a LBM model coupling free gas flow and gas diffusion with adsorption to obtain the dynamic adsorption process of shale gas transport. They reported that

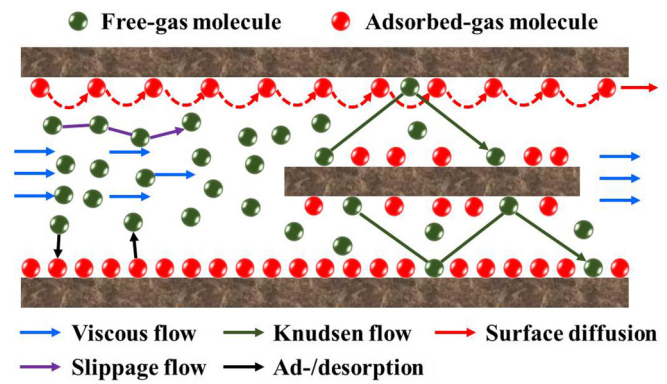


FIG. 1. Schematic of gas flow considering multiphysical fields in shale nanopores.

the increasing adsorption capacity caused by different reasons would have opposite impacts on free gas transport. To reveal the role of adsorbed gas molecules on flow behaviors, Zhao *et al.* [30] employed the quartet structure generation set (QSGS) algorithm to generate a single adsorption layer on the solid surface of porous media and applied the LBM model to simulate the impact of adsorption layer on apparent permeability with different Knudsen numbers. Thereafter, Qu *et al.* [31] introduced gas coverage as the control parameter to quantify the gas molecules adsorbed on the surfaces of the pore body and throat, and then developed a local coupled diffusivity LBM model to study the diffusion behaviors in shale organic matter.

In addition to developing a model at a single scale, multiscale modeling has been proposed to gain comprehensive understanding of the complicated multiphysical fields coupling shale gas transport in shale nanoporous media [32,33]. Yu *et al.* [34] developed a multiscale model with a combination of molecular simulation and pore network model to examine gas flow performances in shale matrix. Li *et al.* [35] proposed a multiscale approach of molecular simulation and REV-scale LBM to investigate the influence of adsorption on gas transport. More recently, Hu and Wang [36] proposed a combination approach of fractal theory and LBM model to examine the shale gas diffusion process in a nanoporous medium. They considered the effects of complex microstructures at the base scale by using the LBM and described the gas diffusion in finer microstructures through fractal theory. In our previous work, a combined molecular simulation and LBM model was developed to study shale gas flow behaviors considering multiple physical fields, i.e., gas adsorption, surface diffusion, and slippage effects, in an organic slit-shaped nanochannel [37]. The results indicated that both surface diffusion and free gas diffusion play the key roles in an organic nanochannel with pore size of 2–20 nm.

In the present work, a multiscale model is developed to explore the gas flow behaviors considering multiple transport mechanisms in shale matrix, including gas slippage, surface diffusion induced by adsorbed gas, and viscous flow, as illustrated in Fig. 1. Molecular simulations are employed to obtain the insightful and underlying gas adsorption characteristics in shale organic nanopore. The adsorption properties are then integrated into a developed pore-scale

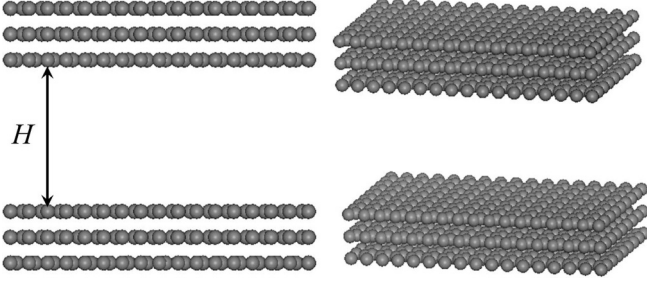


FIG. 2. Graphene slit model of organic nanopore in shale matrix.

MRT-LBM model, in which the multiphysical fields of shale gas transport are taken into consideration. Based on the proposed model, the influences of pressure, temperature, porosity, average pore size, and adsorbed gas molecules on gas transport behaviors in nanoporous shale matrix are investigated and discussed in depth.

II. MODELS AND METHODS

A. Molecular simulations

To obtain the gas adsorption properties in shale organic nanopore, the grand canonical Monte Carlo (GCMC) and molecular dynamics (MD) simulations are first preformed. A three-layer graphene slit model is constructed to represent the organic nanopore of shale formations, as presented in Fig. 2. For methane gas, the spherical united-atom model is applied [38]. The GCMC simulations are carried out for exploring the adsorption characteristics of shale gas in the slit. For each GCMC simulation, a total of 1.1×10^7 Monte Carlo steps are performed, with the first 1×10^6 steps for achieving the equilibrium state and the latter 1×10^7 steps for calculating the physical properties. Then, the MD is adopted to analyze the gas adsorption performances. In molecular simulations, the widely used condensed-phase optimized molecular potentials for atomistic simulation studies force field is utilized [39]. The nonbonded interactions between particles are determined by using the Lennard-Jones (LJ) 9-6 potential function and sixth power combination combining rules [40]. In particular, the Ewald sum algorithm is used for determining the Coulomb

interactions with an accuracy of 1×10^{-3} kcal/mol. The van der Waals interactions are calculated by the atom-based method within a fine cutoff distance of 12.5 Å. All molecular simulations are carried out using the MATERIALS STUDIO package. One can refer to our previous work for more details of gas adsorption in shale nanopores via molecular simulations [11–13,41].

B. Lattice Boltzmann model

Although the lattice Boltzmann model based on the Bhatnagar-Gross-Krook (BGK) collision operator is commonly utilized because of its simplicity and high computational efficiency [42], the inherent deficiencies of the BGK-LBM model, e.g., the numerical instability at low viscosity and inaccuracy in treating boundary conditions, have restricted its applications in practice [43]. In the present study, the MRT-LBM model is employed due to its superior feature in terms of numerical stability and accuracy [44,45]. The evolution equation of MRT-LBM is expressed as

$$\begin{aligned} f(\mathbf{x} + \mathbf{e}_\alpha \delta_t, t + \delta_t) - f(\mathbf{x}, t) \\ = -\mathbf{M}^{-1} \mathbf{S} [m(\mathbf{x}, t) - m^{eq}(\mathbf{x}, t)], \end{aligned} \quad (1)$$

where $f(\mathbf{x}, t) = f_\alpha(\mathbf{x}, t)$ is the particle distribution function (PDF) in the α direction at position \mathbf{x} and time t in velocity space. δ_t denotes the time step. By using the orthogonal transformation matrix \mathbf{M} , the discrete distribution functions in the velocity space can be projected into vectors in the moment space through $\mathbf{m} = \mathbf{M} \cdot \mathbf{f}$ and $\mathbf{m}^{eq} = \mathbf{M} \cdot \mathbf{f}^{eq}$. For the commonly used two-dimensional nine-velocity (D2Q9) LBM model, α varies from 0 to 8, i.e., $\mathbf{f}(\mathbf{x}, t) = [f_0(\mathbf{x}, t), f_1(\mathbf{x}, t), \dots, f_8(\mathbf{x}, t)]^T$ and $\mathbf{m}(\mathbf{x}, t) = [m_0(\mathbf{x}, t), m_1(\mathbf{x}, t), \dots, m_8(\mathbf{x}, t)]^T$. $\mathbf{S} = \text{diag}(\tau_\rho, \tau_e, \tau_e, \tau_j, \tau_j, \tau_q, \tau_q, \tau_s, \tau_s)^{-1}$ is a diagonal relaxation matrix. \mathbf{f}^{eq} is the equilibrium distribution function, which can be written as

$$f_\alpha^{eq} = \rho w_\alpha [1 + (\mathbf{e}_\alpha \cdot \mathbf{u})/c_s^2 + (\mathbf{e}_\alpha \cdot \mathbf{u})^2/2c_s^4 - \mathbf{u}^2/2c_s^2], \quad (2)$$

where w_α is the weighting factor. For the D2Q9 LBM model, the weighting factors are $w_0 = 4/9$, $w_{1-4} = 1/9$, and $w_{5-8} = 1/36$. c_s is the speed of sound ($c_s^2 = c^2/3$). \mathbf{e}_α is the discrete velocity, which is defined as

$$\mathbf{e}_\alpha = \begin{cases} (0, 0) & \alpha = 0 \\ c \{ \cos [(\alpha - 1)\pi/2], \sin [(\alpha - 1)\pi/2] \} & \alpha = 1 - 4 \\ \sqrt{2}c \{ \cos [(2\alpha - 1)\pi/4], \sin [(2\alpha - 1)\pi/4] \} & \alpha = 5 - 8 \end{cases} \quad (3)$$

where $c = \delta_x/\delta_t$ represents the lattice velocity. It is usually set to be unit, while it is adjustable based on different lattice spacing and time step in the LBM model. The transformation matrix \mathbf{M} of the D2Q9 model can be constructed as [43]

$$\mathbf{M} = \begin{pmatrix} 1 & 1 & 1 & 1 & 1 & 1 & 1 & 1 & 1 \\ -4 & -1 & -1 & -1 & -1 & 2 & 2 & 2 & 2 \\ 4 & -2 & -2 & -2 & -2 & 1 & 1 & 1 & 1 \\ 0 & 1 & 0 & -1 & 0 & 1 & -1 & -1 & 1 \\ 0 & -2 & 0 & 2 & 0 & 1 & -1 & -1 & 1 \\ 0 & 0 & 1 & 0 & -1 & 1 & 1 & -1 & -1 \\ 0 & 0 & -2 & 0 & 2 & 1 & 1 & -1 & -1 \\ 0 & 1 & -1 & 1 & -1 & 0 & 0 & 0 & 0 \\ 0 & 0 & 0 & 0 & 0 & 1 & -1 & 1 & -1 \end{pmatrix}. \quad (4)$$

By substituting the equilibrium distribution function f^{eq} given in Eq. (2), the equilibrium distribution function of moment space can be determined as

$$\mathbf{m}^{eq} = \rho [1, -2 + 3u^2, 1 - 3u^2, u_x, -u_x, u_y, -u_y, u_x^2 - u_y^2, u_x u_y]^T, \quad (5)$$

where $\mathbf{u} = (u_x, u_y)$ is the fluid velocity involving the velocities u_x and u_y in the x and y directions, respectively. The macroscopic variables of fluid can be given by

$$\rho = \sum f_\alpha, \quad \mathbf{u} = \frac{1}{\rho} \sum f_\alpha \mathbf{e}_\alpha. \quad (6)$$

For microscale flow, especially in the case of large Knudsen number, inadequate intermolecular collisions between gas molecules and solid wall would result in the molecular mean free path near the wall being smaller than that in the unbounded system, where it is known as the Knudsen layer. For simulating microscale flow in shale reservoir by using the LBM, there are two key issues which should be addressed. First, the relaxation time should be correctly connected to the characteristic parameter Knudsen number. Secondly, appropriate boundary conditions should be chosen to deal with the complex curved boundaries between the fluid and solid surfaces. For the first one, the relationship between the Knudsen number and the relaxation time τ_s proposed by Guo *et al.* [46,47] is adopted in this work:

$$\tau_s = \frac{1}{2} + \sqrt{\frac{6}{\pi}} N \text{Kn}_e, \quad (7)$$

where N denotes the grid number occupied by the characteristic length, and the effective Knudsen number Kn_e can be decided by

$$\text{Kn}_e = \frac{\lambda_e}{H_{\text{local}}}, \quad (8)$$

where H_{local} represents the local pore size due to the random pore size distribution in porous media. λ_e denotes the effective molecular mean free path, which is determined by

$$\lambda_e = \lambda \psi(\text{Kn}), \quad (9)$$

where $\psi(\text{Kn})$ represents the correction function of the Knudsen layer. λ is the molecular mean free path in an unbounded system and is calculated by

$$\lambda = \frac{k_B T}{\sqrt{2} \pi P d^2}, \quad (10)$$

where k_B denotes the Boltzmann constant and d is the diameter of the gas molecule. P and T are the system pressure and temperature, respectively.

In order to enhance the applicability of the LBM model for microflow with large Knudsen number, the calculation for the correction function is crucial. Stops [48] derived an expression for the correction function to describe microflow between two parallel walls, where $\psi(\text{Kn})$ is geometry dependent. However, the distances are difficult to deal with for complex porous media. Thus, Guo *et al.* [46] averaged the Knudsen layer effect into the entire flowing area and proposed a simplified position-independent correction function:

$$\psi(\text{Kn}) = 2 \arctan(\sqrt{2} \text{Kn}^{-3/4}) / \pi. \quad (11)$$

C. Boundary conditions

For developing a LBM model for microflow in porous media, the treatment of a complex curved boundary and the selection of appropriate boundary conditions is another key issue. The main difference between a curved boundary and a straight boundary condition is that the lattice nodes for curved boundaries do not lie on the physical boundary, as shown in Fig. 3(a). For the porous media with irregular boundaries, the midpoint between a fluid node and a solid node $(x_{fb} + x_s)/2$ is usually considered as an approximated wall boundary node [49]. Figure 3(b) illustrates that this approximation reduces the curved physical boundary to a zigzag ghost boundary. The above processing has been considered to be a reasonable choice when the mesh is fine enough [28].

The application of the halfway scheme boundary conditions to the approximate boundary is necessary after completing the curved boundary approximation. The commonly used boundary conditions for capturing the microscale slip effect include the combined bounce-back and specular reflection, full diffusive and specular reflection, and bounce-back and full diffusive scheme [18,19,45]. As the direction of the PDF in the specular reflection scheme is difficult to determine for a curved boundary, the combined bounce-back and full diffusive boundary condition is applied in this study [45,50]. The particle distribution function for the fluid boundary node is expressed as

$$f_\alpha = r K f_\alpha^{eq}(\rho_w, \mathbf{u}_w) + (1 - r) \bar{f}_\alpha, \quad (\mathbf{e}_\alpha - \mathbf{u}_w) \cdot \mathbf{n} > 0, \quad (12)$$

where r represents the combination coefficient for determining the contributions of the bounce-back and full diffusive boundary condition. \mathbf{u}_w is the velocity of a solid wall. In this study, the transport of the shale gas adsorption phase is regarded as a moving solid wall, and thus \mathbf{u}_w is equal to the surface diffusion velocity \mathbf{u}_{surf} . \bar{f}_α is the postcollision particle distribution function, and is defined as $\bar{f}_\alpha =$

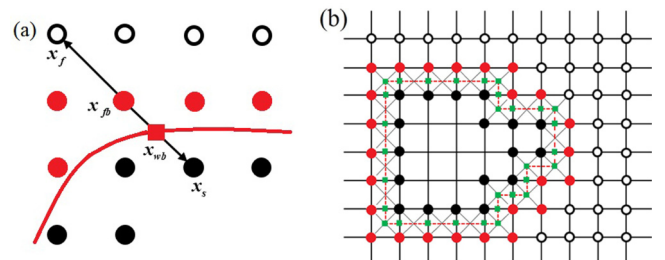


FIG. 3. Schematic of (a) curved boundary and (b) approximated treatment of the curved boundary. The red solid and dashed lines represent the physical boundary and simplified ghost boundary, respectively. The red filled circle is a fluid boundary node with one neighboring solid node at least. The black filled circle is a solid node with one neighboring fluid node at least and the open circle denotes the fluid node. The red and green squares represent the wall boundary node and the approximated wall boundary node, respectively.

TABLE I. Correlations for calculating surface diffusivity [53].

Parameter	Correlation	Notes
D_s^0 , surface diffusivity when gas coverage is 0	$D_s^0 = 8.29 \times 10^{-7} T^{0.5} \exp(-\Delta H^{0.8}/RT)$	R is gas universal constant and T is temperature. ΔH is the isosteric adsorption heat when gas coverage is 0.
$H(1-k)$, Heaviside function	$H(1-k) = \begin{cases} 0 & k \geq 1 \\ 1 & 0 \geq k < 1 \end{cases}$	k is the ratio of blocking velocity coefficient to forward velocity coefficient. Here, we choose $k = 0.5$.
θ , gas coverage	$\theta = bP/(1 + bP)$	θ is derived from Langmuir adsorption theory.

$f_{\bar{\alpha}} - \mathbf{M}^{-1} \mathbf{S} \mathbf{M} [f_{\bar{\alpha}} - f_{\bar{\alpha}}^{eq}]$. $\mathbf{e}_{\bar{\alpha}} = -\mathbf{e}_{\alpha}$ represents two opposite directions of the bounce-back scheme. \mathbf{n} denotes the unit normal vector. The parameter K is defined as

$$K = \frac{\sum_{(\mathbf{e}_{\alpha} - \mathbf{u}_w) \cdot \mathbf{n} < 0} |(\mathbf{e}_{\alpha} - \mathbf{u}_w) \cdot \mathbf{n}| f_{\alpha}}{\sum_{(\mathbf{e}_{\alpha} - \mathbf{u}_w) \cdot \mathbf{n} > 0} |(\mathbf{e}_{\alpha} - \mathbf{u}_w) \cdot \mathbf{n}| f_{\alpha}^{eq}(\rho_w, \mathbf{u}_w)}. \quad (13)$$

To satisfy the second-order slip boundary condition, the combination coefficient and relaxation time are selected as [45]

$$r = \frac{2C_1}{\sqrt{\frac{6}{\pi} + C_1}}, \quad (14)$$

$$\tau_q = \frac{1}{2} + \frac{3 + \pi(2\tau_s - 1)^2 C_2}{8(2\tau_s - 1)}, \quad (15)$$

where $C_1 = 1.11$, $C_2 = 0.61$. By combining the Langmuir adsorption isotherm and the Maxwell-Stefan approach, \mathbf{u}_{surf} is determined as [51]:

$$\mathbf{u}_{\text{surf}} = \frac{q_{\text{sat}} M}{\rho_{\text{ads}}} \frac{b D_s}{1 + bP} \nabla P, \quad (16)$$

where q_{sat} is the Langmuir volume and M denotes the molecular weight of methane. b denotes the Langmuir constant, which is determined by $b = 1/P_L$ with P_L representing the Langmuir pressure. ∇P is the pressure gradient. ρ_{ads} is the density of adsorbed gas. D_s represents the surface diffusivity, which can be determined by using the kinetic method [52]:

$$D_s = D_s^0 \frac{(1 - \theta) + k\theta(2 - \theta)/2 + [H(1 - k)](1 - k)k\theta^2/2}{(1 - \theta + k\theta/2)^2}. \quad (17)$$

The definition and calculation of the parameters in Eq. (17) are listed in Table I. The detailed selections of the parameters can be found in our previous study [37]. It should be noted that, in previous studies, the densities of adsorbed gas were usually set as constant values, e.g., certain times of free gas density [7,27]. In this work, the densities of adsorbed gas are determined by molecular simulations, which are local parameters and related to the pore size, pressure, and temperature of shale formations.

D. Regularization procedure

In the LB model, the projection of the LB equation to Hermite space H^N could introduce an error because the par-

ticle distribution function does not entirely lie within H^N . Previous studies have shown that the error cannot be ignored in large Knudsen flow and porous media [54]. In this study, the regularization procedure is introduced to alleviate this error [55]. With the regularization procedure, the poststreaming distribution function is divided into two parts:

$$f_{\alpha} = f_{\alpha}^{eq} + f_{\alpha}^{neq}, \quad (18)$$

where f_{α}^{eq} and f_{α}^{neq} denote the equilibrium part and the nonequilibrium part, respectively. The nonequilibrium part is transformed into a new distribution function:

$$\bar{f}_{\alpha}^{neq} = w_{\alpha} \left[\frac{1}{2c_s^2} H^{(2)}\left(\frac{\mathbf{e}_{\alpha}}{c_s}\right) \sum_{\beta=0}^{Q-1} f_{\beta}^{neq} e_{\beta i} e_{\beta j} \right], \quad (19)$$

where $H^{(2)}$ represents the second-order Hermite polynomial $H_{ij}^2(\mathbf{e}) = e_i e_j - \delta_{ij}$ and δ_{ij} is the Kronecker delta function. Through the above transformation, the evolution equation of the MRT-LBM becomes

$$\begin{aligned} & f(\mathbf{x} + \mathbf{e}_{\alpha} \delta_t, t + \delta_t) \\ &= f^{eq}(\mathbf{x}, t) + \bar{f}^{neq}(\mathbf{x}, t) - \mathbf{M}^{-1} \mathbf{S} \mathbf{M} \bar{f}^{neq}(\mathbf{x}, t). \end{aligned} \quad (20)$$

III. SHALE ORGANIC MATTER RECONSTRUCTION

To characterize the realistic shale gas reservoir, which is a porous medium composed of multiscale pores and solid matrix, the QSGS algorithm with the advantages of restoring the randomness and irregularity of porous media is adopted to reconstruct the porous structure. The basic idea behind the QSGS method is to grow the selected growth seeds into their neighborhood according to the given growth probabilities of different directions until the reconstructed porous media reach the required porosity. The reconstruction process can be controlled by four parameters, i.e., the core distribution probability, directional growth probability, volume fraction, and phase interaction growth probability [56]. The obtained porous structure of shale organic matter is shown in Fig. 4(a), where the blue and gray parts represent the pore and solid shale matrix, respectively.

In shale organic matter, gas molecules are adsorbed on the solid surface, forming an adsorption layer. As mentioned before, the adsorption layer would affect gas transport in different ways. However, the gas adsorption layer was usually omitted in previous numerical models. To incorporate and examine the influences of the gas adsorption layer, a lattice resolution of 0.4 nm, which is approximately equal

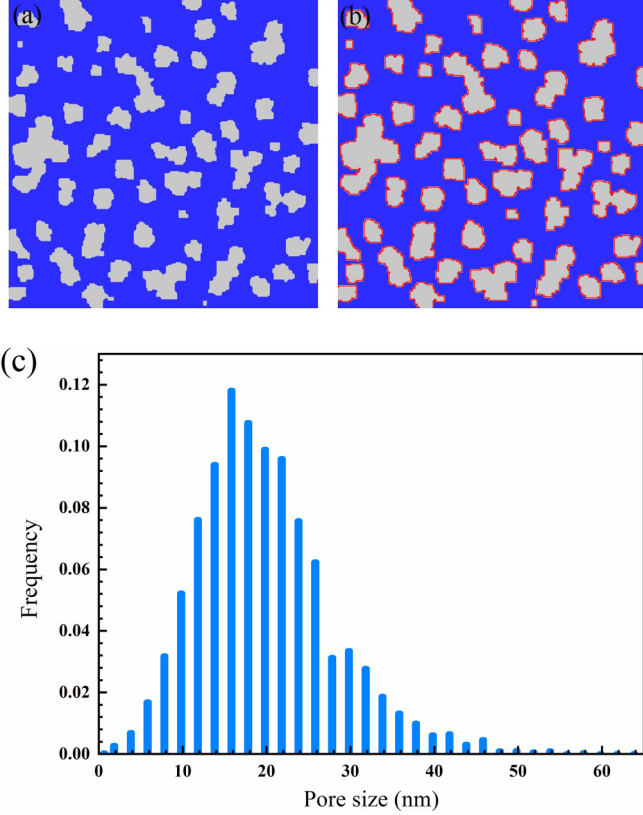


FIG. 4. Schematic of nanopore structure of shale organic matter (a) without and (b) with adsorbed gas molecules (red color); (c) the pore size distribution of nanoporous structure.

to the diameter of a methane molecule, is introduced around the solid matrix to represent shale gas adsorption based on the well accepted Langmuir single-layer adsorption theory, as displayed in Fig. 4(b). The pore size distribution of the nanoporous structure is shown in Fig. 4(c), which is consistent with previous experiment data [57].

In addition to porosity, the average pore size is an important characteristic parameter to determine the local Knudsen numbers of porous structures. Before calculating the average pore size by using Eq. (21), knowing the local pore size at each pore node of porous media is necessary.

$$d_{\text{avg}} = \frac{\sum d_{lp}}{N_{lp}}, \quad (21)$$

where d_{avg} represents the average pore size, d_{lp} is the local pore size of the pore node, and N_{lp} is the number of pore nodes. In this study, the local pore size of a two-dimensional porous structure is solved by applying a modified 13-direction average algorithm [58]. According to the algorithm, the local pore diameter could be determined by averaging the 13 diameters crossing the pore center for a three-dimensional porous medium. As for two-dimensional porous media, the local pore size is the arithmetical average value of the four diameters (A , B , C , D) crossing the pore node, as illustrated in Fig. 5. The maximum and minimum lengths of the four directions are eliminated to avoid the overestimation of local pore size [59].

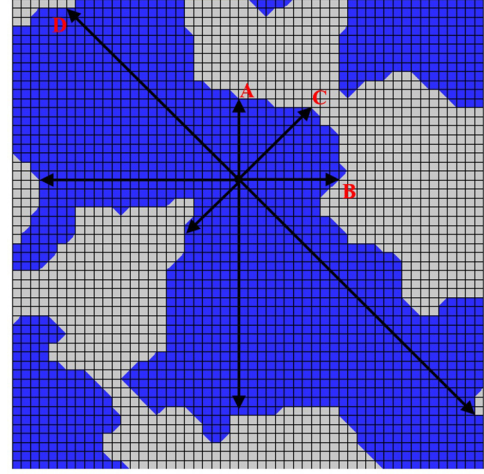


FIG. 5. Schematic of calculating the local pore diameter of porous media.

IV. MODEL VALIDATION

Before investigating gas transport behaviors in nanoporous shale matrix, the developed MRT-LBM model should be verified. First, we simulate gas flow in a microscale channel with the width $H = 4$ nm and length $L = 8$ nm at the conditions of $P = 5$ MPa and $T = 340$ K. The calculated data are compared with those acquired by the direct simulation Monte Carlo (DSMC) and information preservation (IP) methods [60]. For this simulation case, the relaxation times in the model are selected as $\tau_\rho = \tau_j = 1.0$, $\tau_e = 1.1$, and $\tau_\varepsilon = 1.2$. τ_s and τ_q are given by Eqs. (7) and (15). The inlet and outlet of the channel are driven by pressure and the nonequilibrium extrapolation boundary conditions are applied [61]. The combined bounce-back and full diffusive boundary condition is used on the upper and lower walls. The comparisons of normalized velocity profiles for different Knudsen numbers are shown in Fig. 6. The results indicate that the simulated results obtained by the proposed model are in good agreement with those of DSMC and IP results, which could verify the capability to capture slip velocity for simulating gas flow in nanoscale pores.

To further validate the accuracy of the proposed model for nanoporous structure, a microchannel with a square cylinder placed in the center is focused, as displayed in Fig. 7. The heights of the channel and cylinder are set as H and $0.2H$, respectively. The length of the channel is also set as H and the periodic boundary conditions are employed at the inlet and outlet [62]. The size of the simulation domain is 100×100 lattice units (LUs). Figure 8 shows the comparisons of normalized velocity profiles between the LBM and MD simulation results. It is observed that the LBM results generally agree with the MD results. The major difference occurs at the center region with the LBM model predicting the recovery of the velocity deficit after the cylinder faster than the MD simulation. Similar results have been reported in previous work [62]. Therefore, the ability and accuracy of the developed LBM model with regularization procedure in studying gas transport behaviors in nanoporous media have been validated.

In LBM simulations, to ensure the validation and accuracy of the model, the conversions between lattice and physical

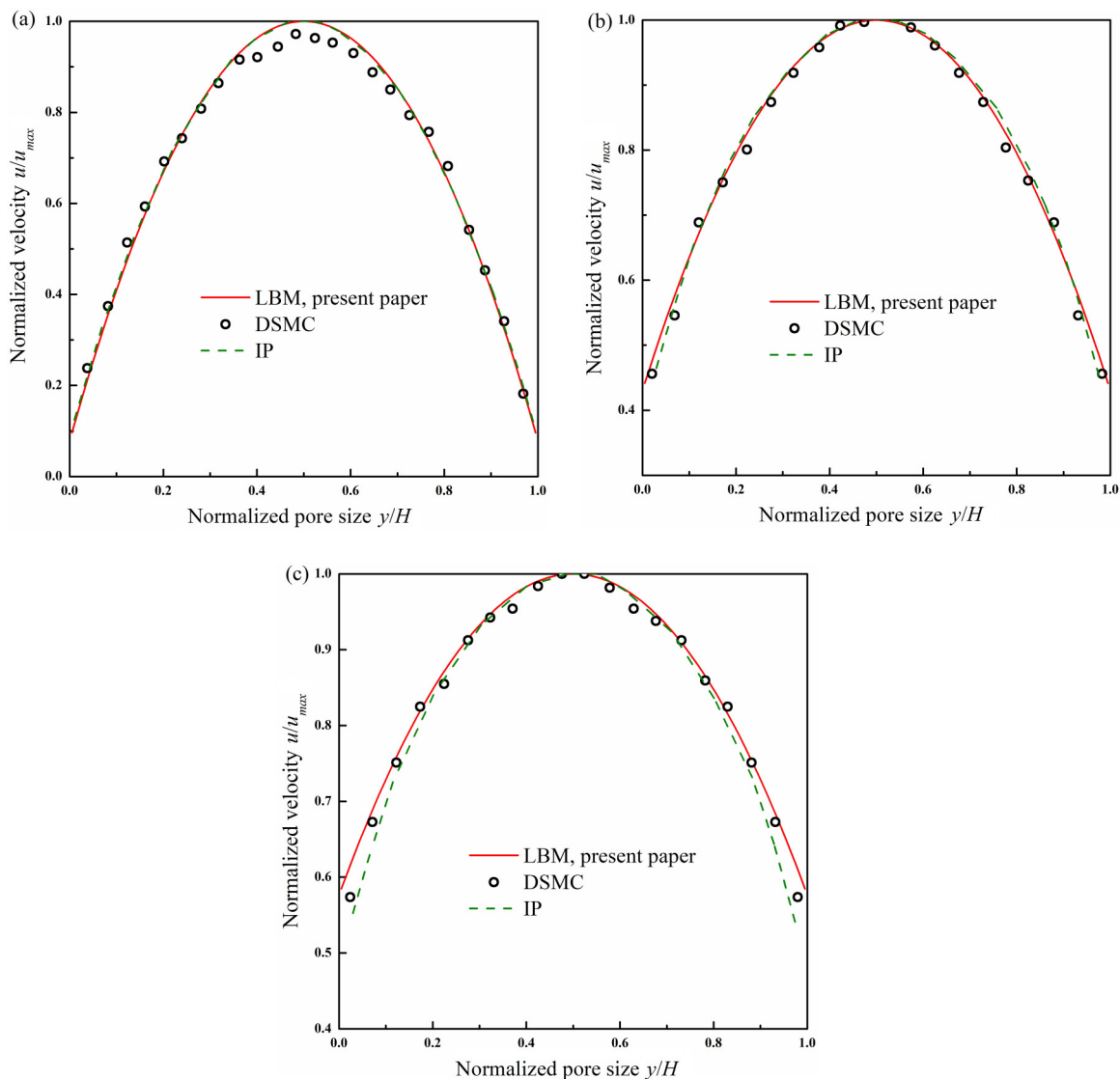


FIG. 6. Comparisons of normalized velocity profiles for different Knudsen numbers: (a) $Kn = 0.0194$; (b) $Kn = 0.194$; (c) $Kn = 0.388$.

units are critical. One can refer to our previous study for detailed procedures for the unit conversion [37].

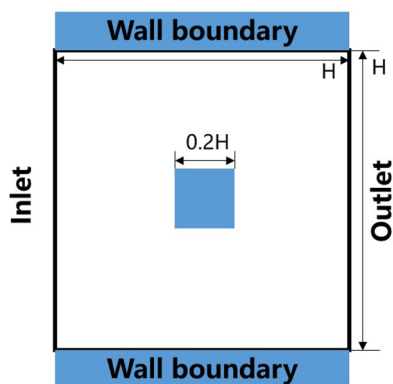


FIG. 7. Schematic of a microscale channel with a square cylinder.

V. RESULTS AND DISCUSSION

A. Gas adsorption behaviors in organic nanopore

Molecular simulations are first performed to examine the influences of temperature, pressure, and pore size on gas adsorption performances in an organic slit-shaped nanopore, as shown in Fig. 2. The validation for molecular simulation investigating gas adsorption in organic and inorganic slit nanopores can be found in our previous work [11,12,41]. Figure 9 displays the relative concentration profiles of shale gas, i.e., the ratio of local to bulk gas concentration, in the nanopores with pore size of 2–10 nm. It is found that the gas concentrations close to the wall are significantly higher than that of the middle area of the pore, indicating that two adsorption layers are formed along the wall. In addition, for the nanopore with pore size of 2–4 nm, secondary adsorption layers could be observed near the primary adsorption layers. It can be ascribed to the coexistence of Langmuir single-layer adsorption and pore-filling adsorption mechanisms due to the confinement effect in nanoscale pore. With the increment of

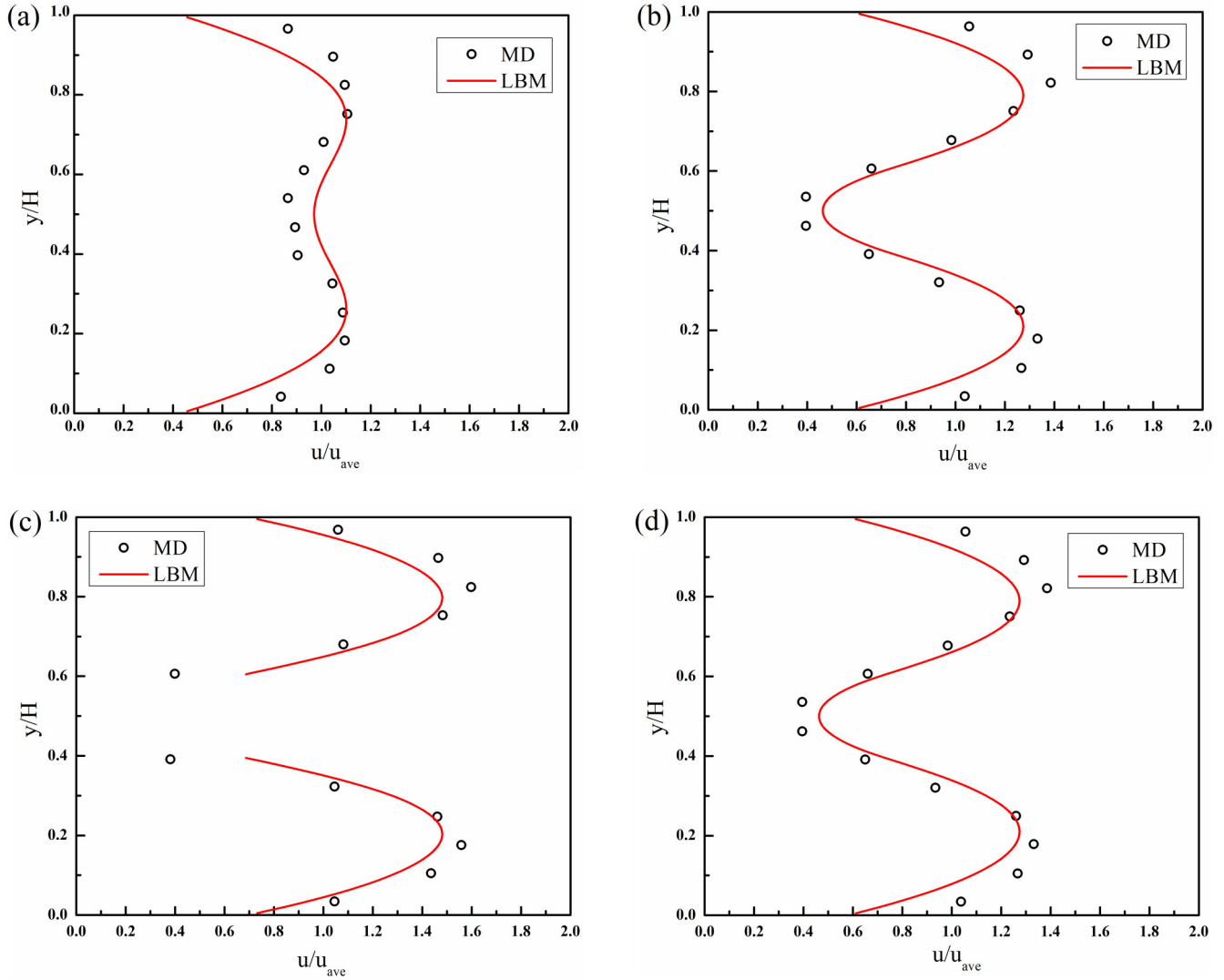


FIG. 8. Comparisons of normalized velocity profiles of the LBM and MD results at different positions of the channel: (a) $x/H = 0$; (b) $x/H = 1/4$; (c) $x/H = 1/2$; (d) $x/H = 3/4$.

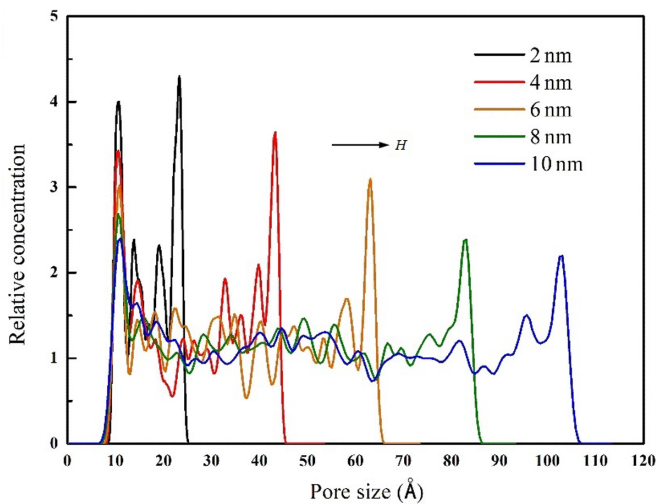


FIG. 9. The gas relative concentration profiles in shale organic nanopore with different pore sizes: $T = 340$ K, $P = 30$ MPa.

pore size, the confinement effect would be gradually weakened, which has been reported in our previous studies [11, 12]. With the further increase of pore size (> 10 nm), it is supposed that the confinement effect is negligible and the density ratios will remain unchanged. The calculated density ratios are shown in Table II. It is observed that the density ratios of adsorbed and free gas are influenced by the adsorption mechanisms, which would be greatly affected by the pressure and pore size (< 10 nm) of nanopores. The obtained gas adsorption characteristics will be incorporated in the LBM model through the local gas adsorption density parameter of boundary conditions as described in Sec. II.

B. Effect of pressure and temperature

During the exploitation process of shale gas, the behaviors of gas transportation would be strongly related with the variations of temperature and pressure. Thus, a series of simulation cases is conducted to reveal their impacts on gas flow in this section. A relatively high porosity of 0.7 is set to reduce

TABLE II. The density ratios of adsorbed and free gas for different pore sizes and pressures; $T = 340$ K.

Pressure (MPa)	Pore Size (nm)				
	2	4	6	8	10
10	2.794	7.567	6.536	5.136	5.085
15	2.956	4.315	4.134	3.408	3.371
20	2.786	3.485	3.642	3.075	2.774
25	2.462	3.174	2.821	2.644	2.154
30	2.363	3.425	2.684	2.132	2.100
35	2.502	2.941	2.785	2.257	2.064
40	2.408	2.408	2.023	2.148	2.018
45	2.369	2.486	2.31	2.045	1.693

dead pores and enhance structural connectivity of the porous structure, as shown in Fig. 4. In the simulations, the domain size for porous media is set as 250×250 LUs with a lattice resolution of 0.4 nm. Gas flow is driven by a fixed pressure gradient of 0.1 MPa/m. The nonequilibrium extrapolation boundary conditions are employed at the inlet and outlet, and periodic boundary conditions are adopted for the upper and lower walls. The proposed combination of bounce-back and full diffusive boundary condition, which incorporates the local gas adsorption density, is applied for dealing with fluid-solid interfaces. The parameter settings in the following calculations remain unchanged, unless otherwise stated.

In order to examine gas transport in realistic shale formation, here we simulate gas flow behaviors under typical reservoir conditions with temperature of 298–385 K and pressure of 5–40 MPa. Figure 10 presents the velocity contours under different pressures. It is apparent that shale gas in the porous structure flows in free space and bypasses the solid matrix, and gas flow velocities in small pores are higher than that in larger pores. Figure 11 illustrates the effects of pressure on the velocity profile at the midpoint of the flow direction ($x/L = 0.5$). There is a clear trend that gas velocity declines with the increasing pressure and gas transport is significantly weakened under high pressures (>30 MPa). This indicates

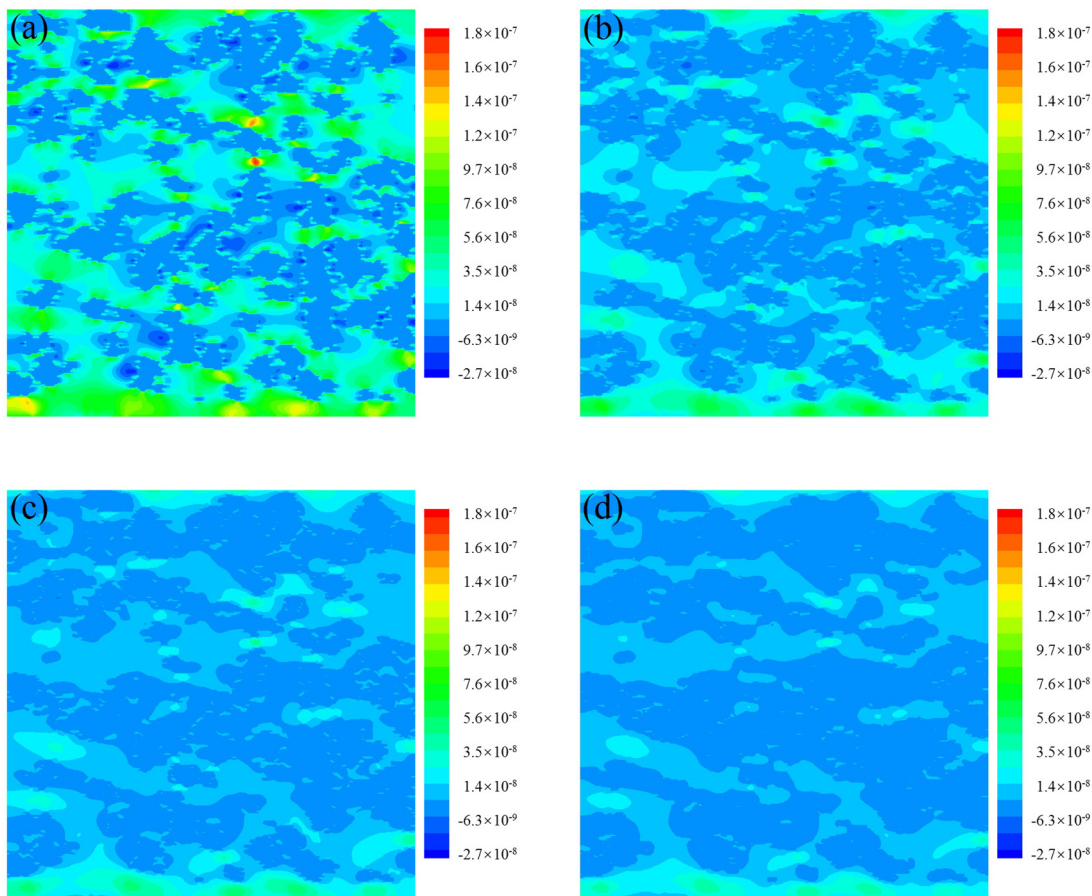


FIG. 10. Velocity contour in nanoporous shale matrix under different pressures: (a) $P = 10$ MPa; (b) $P = 20$ MPa; (c) $P = 30$ MPa; (d) $P = 40$ MPa, $T = 340$ K.

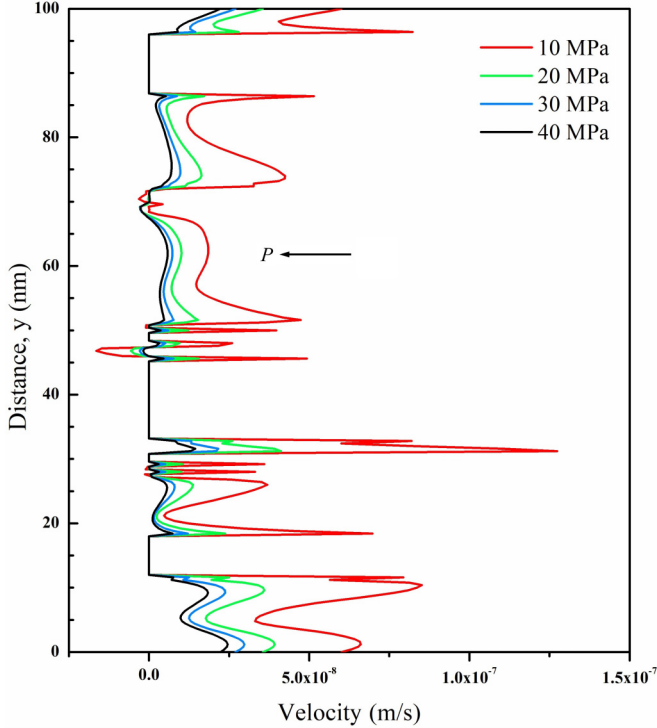


FIG. 11. Gas velocity profiles at $x/L = 0.5$ under different pressures.

that pressure has a great influence on shale gas transportation velocity, especially for lower pressure, which is consistent with the results in a shale organic nanopore in our previous study [37].

In addition to velocity distribution, the apparent permeability K_{app} associated with shale gas production should be addressed, which can be expressed as

$$K_{app} = \frac{u_{ave}\mu}{\nabla P}, \quad (22)$$

where u_{ave} represents the gas average velocity and μ is the kinematic viscosity. To quantitatively describe the effects of pressure and temperature on shale gas production, the apparent permeabilities at different pressures and temperatures are calculated, as plotted in Fig. 12. It is observed that the apparent permeability declines with the increase of pressure, which is in line with the trend of gas velocity. It might be due to the fact that the decrease of mean free path and increase of molecular number density caused by the increasing pressure result in attenuation of the microscale effect and enlargement of flow resistance, which could decrease the gas velocity and apparent permeability. Additionally, it can be seen from the figure that the increasing temperature is beneficial for improving the apparent permeability, but its influence on gas transport is much less than that of pressure. The apparent permeability only increases by 73% with the temperature increasing from 298 to 385 K at the pressure of 5 MPa, while the apparent permeability has a threefold increase with the pressure decreasing from 40 to 5 MPa at the temperature of 298 K.

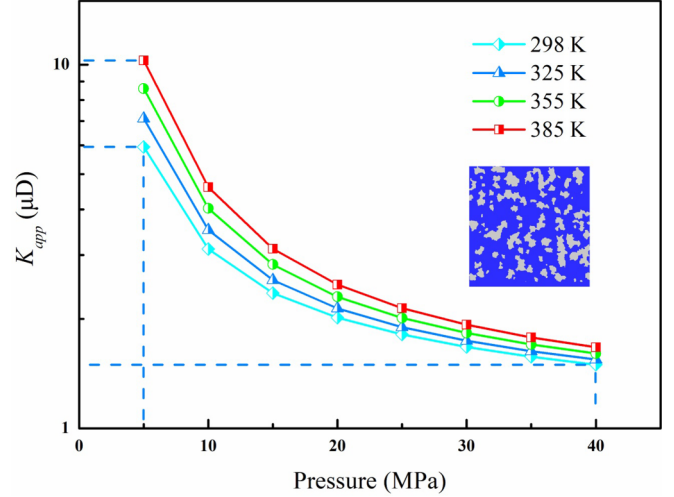


FIG. 12. Variation of apparent permeability with temperature and pressure.

C. Effect of porosity and average pore size

Gas flow behaviors in porous media greatly depend on the morphological characteristics of pore structure. The porosity and average pore size are the important parameters to distinguish different porous shale matrix. To examine the roles of porosity and average pore size on shale gas transportation, here we reconstruct two groups of different porous structures. First, the effects of average pore size on gas transport are focused. Five porous structures with the same porosity but different average pore sizes are reconstructed, as demonstrated in Fig. 13. It is observed that the decreasing average pore size corresponds to more dense solid matrix and tortuous flow path. The constant temperature $T = 340$ K and pressure $P = 10$ MPa are maintained in the calculations. Figure 14 shows the variation of apparent permeability with average pore size. It is found that the apparent permeability increases significantly with the increasing average pore size. This can be ascribed to the fact that the reduced average pore size leads to smaller flow space and more tortuous flow path of free gas, which could greatly hinder the gas transportation in shale matrix.

Secondly, the influences of porosity on gas transport behaviors are studied. Six groups of porous structures with different porosities but the very close average pore size are generated. In addition, to alleviate the errors caused by randomly constructed porous media, three porous structures are generated for each group. The structural parameters are given in Table III. Figure 15 illustrates the variation of apparent permeability with porosity. It is found that the apparent permeability

TABLE III. Structural parameters of reconstructed porous structure with different porosities and average pore size around 16 nm.

Structure	P1	P2	P3	P4	P5	P6
Porosity	0.60	0.65	0.70	0.75	0.80	0.85
Average pore size (nm)	15.9	15.7	16.0	16.1	16.0	15.9
	15.8	16.2	16.1	16.0	16.1	15.9
	16.0	15.9	16.1	16.0	16.1	16.0

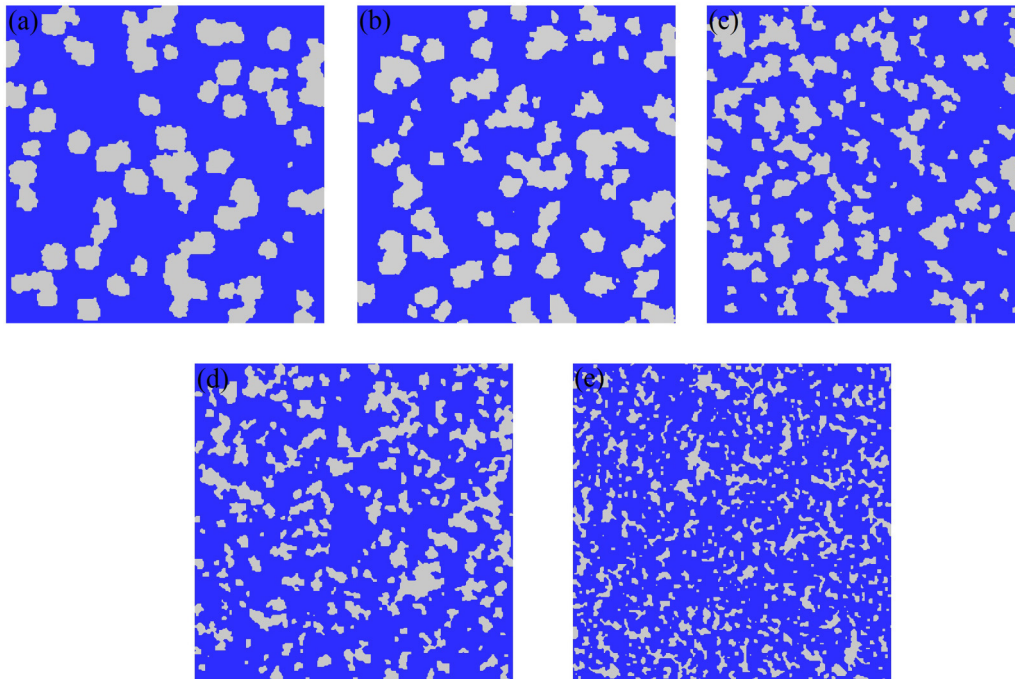


FIG. 13. The reconstructed porous structures with the same porosity of 0.70 but different average pore sizes: (a) $d_p = 23.1$ nm; (b) $d_p = 19.1$ nm; (c) $d_p = 15$ nm; (d) $d_p = 11.1$ nm; (e) $d_p = 6.8$ nm.

slightly increases with the increment of porosity. However, the influences of porosity on apparent permeability are much smaller than that of average pore size. Therefore, in practical applications, both porosity and pore size distribution should be addressed to accurately predict gas transport behavior in shale formations.

D. Effect of gas adsorption layer

Gas in shale matrix mainly exists in the form of free and adsorbed states, in which the adsorbed gas accounts for

about 20%–80% depending on the maturity of the shale organic matter. Therefore, gas adsorption properties could have a great impact on gas transport. In order to fully consider the effects of the existence of the adsorption layer on shale gas transportation, an additional layer is constructed onto the solid matrix to represent the gas adsorption layer. Figure 16 shows the gas velocity contour for four simulation cases with and without considering surface diffusion and adsorbed gas molecules. It is observed that when the adsorbed gas layer is taken into consideration, gas transport could be hindered with the obvious decrease of gas velocity. It can be attributed to the gas adsorption layer reducing the space of free gas and

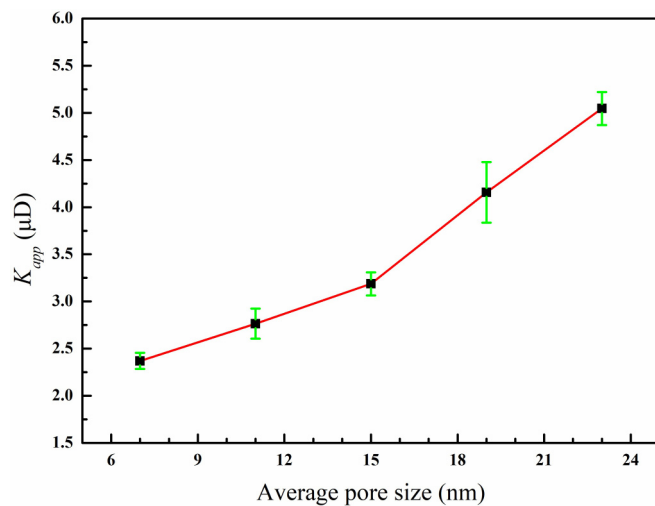


FIG. 14. Variation of apparent permeability with average pore size of porous structure (error bars representing standard deviation of simulation results by three independent reconstructed porous structures with the same parameters, similarly hereinafter).

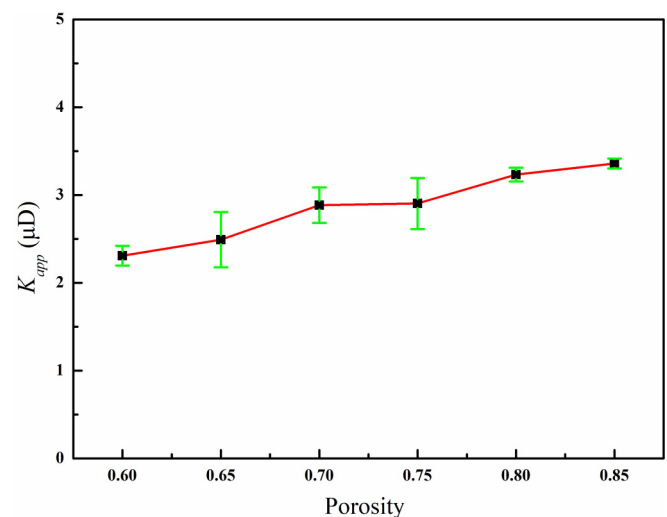


FIG. 15. Variation of apparent permeability with porosity.

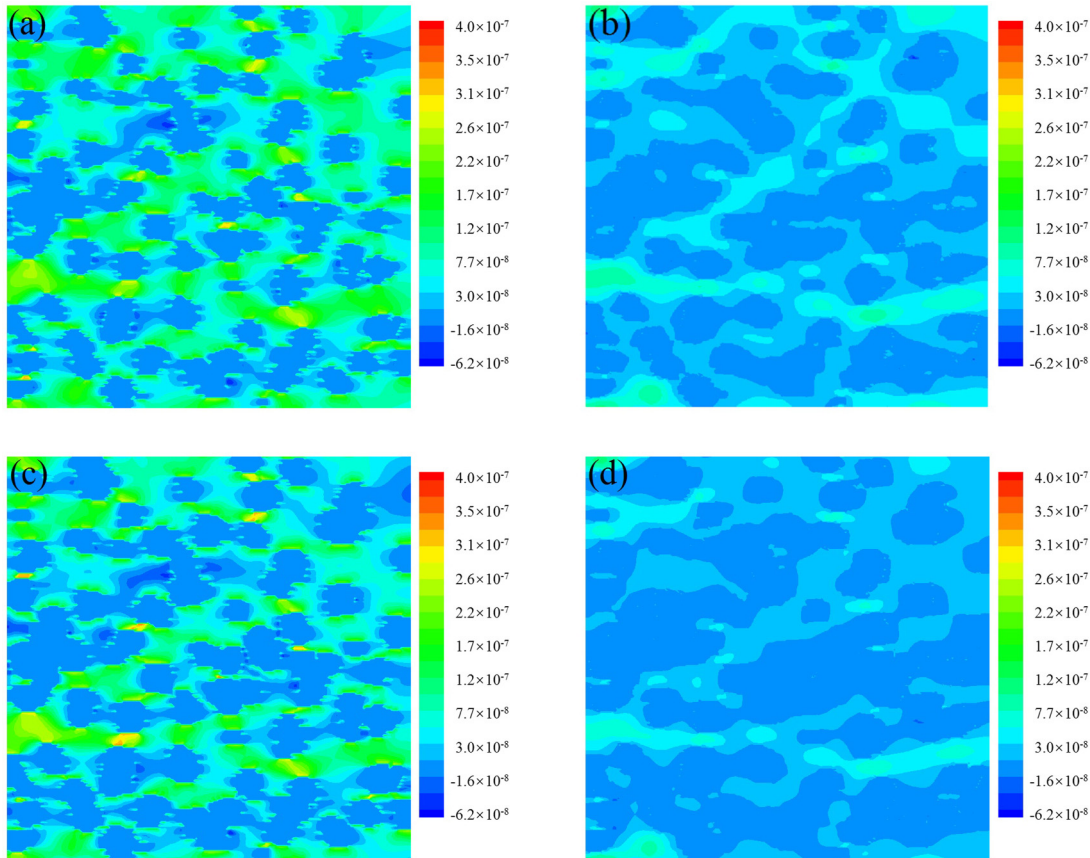


FIG. 16. Velocity contour of four cases: (a) with surface diffusion only; (b) without adsorbed gas and surface diffusion; (c) with adsorbed gas and surface diffusion; (d) with adsorbed gas only; $P = 10$ MPa, $T = 340$ K.

increasing the flow resistance. However, with the consideration of surface diffusion, it can be seen that gas flow velocity could be significantly enhanced.

Furthermore, the effects of the adsorption layer on the apparent permeability at different pressures is quantitatively presented in Fig. 17. First, it can be seen that the pressure has little effect on apparent permeability without considering surface diffusion (cases 1 and 4), while the apparent permeability in cases 2 and 3 decreases significantly with the increase of pressure.

This indicates that surface diffusion in nanoporous shale matrix could promote shale gas transport, with more pronounced influence under low pressure (< 15 MPa). Similar conclusions have been reported in a shale organic nanopore in a previous study [37]. Compared with cases 3 and 4, it can be concluded that the positive effect of surface diffusion on shale gas transport is greater than the negative effect of an adsorbed gas layer under low pressures; therefore the overall effect of the adsorption layer is to increase the apparent permeability. However, as the pressure increases, the trend would be opposite. Beyond a certain value (around 22.5 MPa), the existence of an adsorption layer would reduce the apparent permeability. The reason might be that the increase of pressure will increase the collision between gas molecules, thus reducing the average free path of molecules. The weakened jumping of gas molecules on a solid wall leads to the decrease of surface diffusion. Therefore, it is crucial to employ the appropriate

multiscale model for accurate prediction of gas transport behaviors in shale matrix. These results could also be helpful on developing strategies of shale gas recovery enhancement based on the real-time and realistic reservoir conditions.

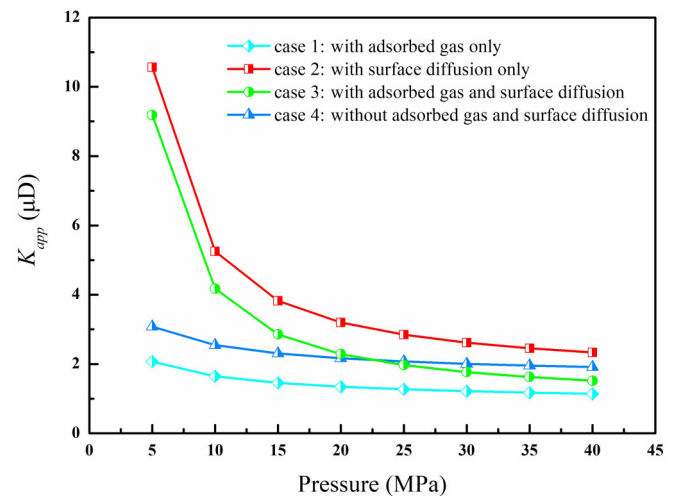


FIG. 17. Variation of apparent permeability with pressure for different cases with and without considering surface diffusion and adsorbed gas layer; $T = 340$ K.

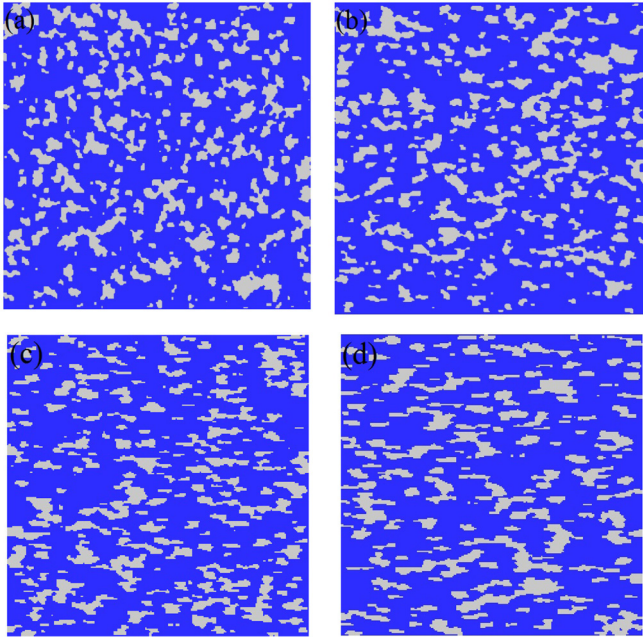


FIG. 18. The anisotropic porous structure with the aspect ratio of (a) $D_{ix}/D_{iy} = 1$; (b) $D_{ix}/D_{iy} = 10$; (c) $D_{ix}/D_{iy} = 40$; (d) $D_{ix}/D_{iy} = 80$.

E. Effect of anisotropy

The porous structure of shale matrix is complicated, showing strong heterogeneity and anisotropy, which is usually caused by the directional arrangement or bedding of clay minerals and microcracks [63]. To reveal the effect of anisotropy, the QSGS method is utilized to generate porous media with different structures. By adjusting the ratio of horizontal to vertical growth probability (also referred to the aspect ratio D_{ix}/D_{iy}), the porous structures with constant porosity of 0.7 and the anisotropy characteristic parallel to flow direction are constructed, as displayed in Fig. 18. It can be seen that the larger the aspect ratio is, the stronger the stratification of porous structure in the x direction is. Figure 19 demonstrates the variation of the apparent permeability in the x direction, i.e., the flow direction, of shale gas with the aspect ratio of porous media. A remarkable increase of the apparent permeability is observed at the beginning, and it gradually increases with the increase of aspect ratio D_{ix}/D_{iy} . It is due to the flow paths in a porous structure with a larger aspect ratio tending to be horizontal and less curved, leading to a lower resistance at the gas flow direction.

VI. CONCLUSIONS

In the present work, we develop a multiscale model combining molecular simulation and a pore-scale MRT-LBM model for investigating gas transport behaviors in nanoporous shale matrix. Gas adsorption characteristics are first explored by applying molecular simulations. Then, the gas adsorption properties are integrated in the pore-scale LBM model through a local adsorption density parameter of boundary conditions. The regularization procedure is adopted in the MRT-LBM model to alleviate the error

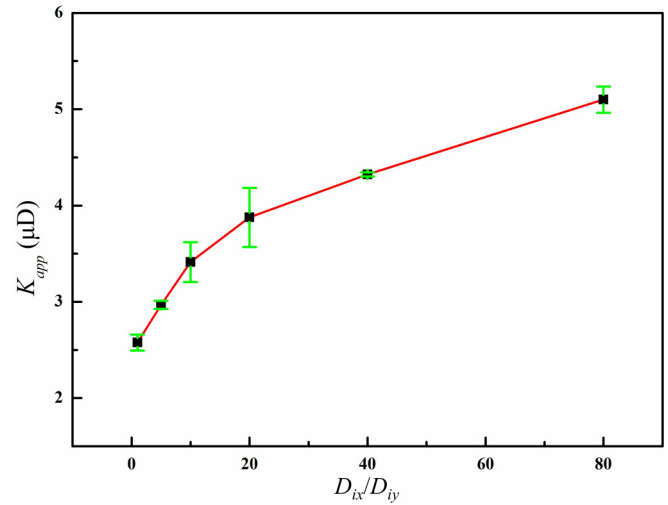


FIG. 19. Variation of apparent permeability in the flow direction with aspect ratio D_{ix}/D_{iy} of anisotropic porous structure; $P = 10$ MPa, $T = 340$ K.

caused by high Knudsen number and nanoporous structure. The combined bounce-back and full diffusive boundary condition is introduced to take account of gas slippage and surface diffusion effects. An external layer is generated on the solid surface of the shale matrix to consider the influences of the gas adsorption layer. The proposed model has been validated by comparing with molecular simulations and other algorithms. The influences of temperature, pressure, pore network, and adsorption layer on gas transport considering multiphysical fields, including gas adsorption, gas slippage, and surface diffusion, are examined and discussed in detail.

Molecular simulation results show that pressure and pore size have a great impact on the gas adsorption behaviors in shale organic nanopores. With high pressure in small nanoscale pores (< 4 nm), the coexistence of Langmuir single-layer and pore-filling adsorptions are found due to the confinement effects. Therefore, it can be concluded that the gas adsorption behaviors have strong relationships to pressure and pore size of shale nanopores, which should be taken into consideration when gas transport is examined in shale matrix.

Numerical simulation results by the proposed multiscale model indicate that a higher temperature and lower pressure could help improve the gas apparent permeability. Compared to temperature, pressure has more remarkable impact on gas transport behaviors within the studied range. A three-fold increase of apparent permeability has been found with the pressure decreasing from 40 to 5 MPa. In addition, the effects of average pore size are more significant than that of porosity of shale porous media. Both pore size distribution and porosity of shale reservoirs should be taken into consideration for studying gas transport behaviors in shale reservoirs. Moreover, under lower pressure, the positive effect of the gas adsorption layer, i.e., surface diffusion, is found to be greater than its negative effect, leading the enhancement of the overall apparent permeability. The results show that a proper boundary condition, which takes account of the adsorption layer and gas slippage as well as surface

diffusion, is crucial for accurately describing gas transport in shale nanoporous formations. Otherwise, the apparent permeability would be obviously over- or underestimated. Lastly, the anisotropy characteristic along the flow direction of the nanoporous structure is conducive to enhancing gas transport in shale formations.

ACKNOWLEDGMENTS

This work was supported by the National Natural Science Foundation of China (Grant No. 51706018) and the Fundamental Research Funds for the Central Universities (Grants No. FRF-TP-19-009A3 and No. FRF-BD-20-09A).

-
- [1] J. Q. Norris, D. L. Turcotte, and J. B. Rundle, *Phys. Rev. E* **89**, 022119 (2014).
- [2] R. J. Ambrose, R. C. Hartman, M. Diaz-Campos, I. Y. Akkutlu, and C. H. Sondergeld, *SPE J.* **17**, 219 (2012).
- [3] C. W. MacMinn, E. R. Dufresne, and J. S. Wettlaufer, *Phys. Rev. X* **5**, 011020 (2015).
- [4] A. Papaioannou and R. Kausik, *Phys. Rev. Appl.* **4**, 024018 (2015).
- [5] R. Krishna and J. A. Wesselingh, *Chem. Eng. Sci.* **52**, 861 (1997).
- [6] P. Tahmasebi, F. Javadpour, and M. Sahimi, *Transp. Porous Media* **110**, 521 (2015).
- [7] H. Yu, J. Chen, Y. Zhu, F. Wang, and H. Wu, *Int. J. Heat Mass Transfer* **111**, 1172 (2017).
- [8] F. Chen, S. Lu, X. Ding, X. He, and H. Xing, *J. Petrol. Sci. Eng.* **160**, 207 (2018).
- [9] L. Xu, M. G. Sedigh, M. Sahimi, and T. T. Tsotsis, *Phys. Rev. Lett.* **80**, 3511 (1998).
- [10] D. Mantzalis, N. Asproulis, and D. Drikakis, *Phys. Rev. E* **84**, 066304 (2011).
- [11] W. Zhou, H. Wang, X. Yang, X. Liu, and Y. Yan, *Ind. Eng. Chem. Res.* **59**, 6696 (2020).
- [12] W. Zhou, H. Wang, Y. Yan, and X. Liu, *Energy Fuels* **33**, 6542 (2019).
- [13] W. Zhou, Z. Zhang, H. Wang, and X. Yang, *Nanomaterials* **9**, 1646 (2019).
- [14] T. Wang, S. Tian, G. Li, L. Zhang, M. Sheng, and W. Ren, *Renew. Sustain. Energy Rev.* **149**, 111391 (2021).
- [15] H. Wang, Z. Qu, Y. Yin, J. Bai, and B. Yu, *J. Therm. Sci.* **28**, 1 (2019).
- [16] Y.-L. He, Q. Liu, Q. Li, and W.-Q. Tao, *Int. J. Heat Mass Transfer* **129**, 160 (2019).
- [17] Q. Li, K. H. Luo, Q. J. Kang, Y. L. He, Q. Chen, and Q. Liu, *Prog. Energy Combust. Sci.* **52**, 62 (2015).
- [18] S. Succi, *Phys. Rev. Lett.* **89**, 064502 (2002).
- [19] G. H. Tang, W. Q. Tao, and Y. L. He, *Phys. Fluids* **17**, 058101 (2005).
- [20] C. K. Aidun and J. R. Clausen, *Annu. Rev. Fluid Mech.* **42**, 439 (2010).
- [21] J. Ren, Q. Zheng, P. Guo, and C. Zhao, *Entropy* **21**, 133 (2019).
- [22] Z. Guo and T. S. Zhao, *Phys. Rev. E* **66**, 036304 (2002).
- [23] L. Chen, W. Fang, Q. Kang, J. De'Haven Hyman, H. S. Viswanathan, and W.-Q. Tao, *Phys. Rev. E* **91**, 033004 (2015).
- [24] A. Beskok and G. E. Karniadakis, *Microscale Thermophys. Eng.* **3**, 43 (1999).
- [25] F. Civan, *Transp. Porous Media* **82**, 375 (2010).
- [26] J. Wang, Q. Kang, Y. Wang, R. Pawar, and S. S. Rahman, *Fuel* **205**, 232 (2017).
- [27] Y. Ning, Y. Jiang, H. Liu, and G. Qin, *J. Nat. Gas Sci. Eng.* **26**, 345 (2015).
- [28] J. Ren, P. Guo, S. Peng, and C. Yang, *J. Nat. Gas Sci. Eng.* **29**, 169 (2016).
- [29] T. Zhang and S. Sun, *Fuel* **246**, 196 (2019).
- [30] T. Zhao, H. Zhao, X. Li, Z. Ning, Q. Wang, W. Zhao, and J. Zhang, *Chem. Eng. Sci.* **187**, 245 (2018).
- [31] Z. G. Qu, Y. Yin, H. Wang, and J. F. Zhang, *Fuel* **260**, 116423 (2020).
- [32] A. Božan, F.-J. Ulm, R. J.-M. Pellenq, and B. Coasne, *Phys. Rev. E* **91**, 032133 (2015).
- [33] P. Tahmasebi, F. Javadpour, M. Sahimi, and M. Piri, *Adv. Water Resour.* **89**, 91 (2016).
- [34] H. Yu, Y. Zhu, X. Jin, H. Liu, and H. Wu, *J. Nat. Gas Sci. Eng.* **64**, 28 (2019).
- [35] Z.-Z. Li, T. Min, Q. Kang, Y.-L. He, and W.-Q. Tao, *Int. J. Heat Mass Transfer* **98**, 675 (2016).
- [36] B. Hu and J. G. Wang, *Phys. Rev. E* **104**, 065304 (2021).
- [37] X. Yang, W. Zhou, X. Liu, and Y. Yan, *Energy* **210**, 118547 (2020).
- [38] M. G. Martin and J. I. Siepmann, *J. Phys. Chem. B* **102**, 2569 (1998).
- [39] H. Sun, *J. Phys. Chem. B* **102**, 7338 (1998).
- [40] H. Heinz, R. A. Vaia, B. L. Farmer, and R. R. Naik, *J. Phys. Chem. C* **112**, 17281 (2008).
- [41] W. Zhou, Z. Zhang, H. Wang, Y. Yan, and X. Liu, *RSC Adv.* **8**, 33939 (2018).
- [42] Y. Qian, D. d'Humieres, and P. Lallemand, *EPL* **17**, 479 (1992).
- [43] P. Lallemand and L. S. Luo, *Phys. Rev. E* **61**, 6546 (2000).
- [44] D. d'Humières, in *Rarefied Gas Dynamics: Theory and Simulations*, edited by B. D. Shizgal and D. P. Weaver, Progress in Astronautics and Aeronautics Vol. 159 (AIAA, Reston, VA, 1992), p. 450.
- [45] Z. Chai, B. Shi, Z. Guo, and J. Lu, *Commun. Comput. Phys.* **8**, 1052 (2010).
- [46] Z. Guo, T. Zhao, and Y. Shi, *J. Appl. Phys.* **99**, 074903 (2006).
- [47] Z. Guo, C. Zheng, and B. Shi, *Phys. Rev. E* **77**, 036707 (2008).
- [48] D. W. Stops, *J. Phys. D: Appl. Phys.* **3**, 685 (1970).
- [49] A. J. C. Ladd, *J. Fluid Mech.* **271**, 285 (1994).
- [50] Z. H. Chai, Z. L. Guo, L. Zheng, and B. C. Shi, *J. Appl. Phys.* **104**, 014902 (2008).
- [51] J. Wang, Q. Kang, L. Chen, and S. S. Rahman, *Int. J. Coal Geol.* **169**, 62 (2017).
- [52] Y. Chen and R.-T. Yang, *AIChE J.* **37**, 1579 (1991).
- [53] K. Wu, X. Li, C. Wang, W. Yu, and Z. Chen, *Ind. Eng. Chem. Res.* **54**, 3225 (2015).
- [54] K. Suga, *Fluid Dyn. Res.* **45**, 034501 (2013).
- [55] J. Latt and B. Chopard, *Math. Comput. Simul.* **72**, 165 (2006).
- [56] M. Wang, J. Wang, N. Pan, and S. Chen, *Phys. Rev. E* **75**, 036702 (2007).
- [57] M. Shi, B. Yu, Z. Xue, J. Wu, and Y. Yuan, *J. Nat. Gas Sci. Eng.* **26**, 948 (2015).

- [58] K. J. Lange, P.-C. Sui, and N. Djilali, *J. Electrochem. Soc.* **157**, B1434 (2010).
- [59] Y. Yin, Z. G. Qu, and J. F. Zhang, *Int. J. Heat Mass Transfer* **143**, 118571 (2019).
- [60] C. Shen, D. B. Tian, C. Xie, and J. Fan, *Microscale Thermophys. Eng.* **8**, 423 (2004).
- [61] Z. Guo, C. Zheng, and B. Shi, *Phys. Fluids* **14**, 2007 (2002).
- [62] K. Suga, S. Takenaka, T. Ito, M. Kaneda, T. Kinjo, and S. Hyodo, *Phys. Rev. E* **82**, 016701 (2010).
- [63] L. Germanou, M. T. Ho, Y. Zhang, and L. Wu, *J. Nat. Gas Sci. Eng.* **60**, 271 (2018).